Acta Materialia 291 (2025) 120947

Contents lists available at ScienceDirect

Acta Materialia

journal homepage: www.elsevier.com/locate/actamat

Full length article

# Generative 3D reconstruction of Ti-6Al-4V basketweave microstructures by optimization of differentiable microstructural descriptors

Vincent Blümer [a,*], Ali Reza Safi [b], Celal Soyarslan [a,c], Benjamin Klusemann [b,d], Ton van den Boogaard [a]

[a] Nonlinear Solid Mechanics, University of Twente, Drienerlolaan 5, Enschede, 7522 NB, The Netherlands
[b] Institute of Material and Process Design, Helmholtz-Zentrum Hereon, Max–Planck-Straße 1, Geesthacht, 21502, Germany
[c] Fraunhofer Innovation Platform for Advanced Manufacturing, University of Twente, Hengelosestraat 701, Enschede, 7521 PA, The Netherlands
[d] Institute for Production Technology and Systems, Leuphana University Lüneburg, Universitätsallee 1, Lüneburg, 21335, Germany

ARTICLE INFO

Dataset link: https://github.com/vbluemer/MCRpy

*Keywords:*
Microstructure characterization and reconstruction
Convolutional Neural Network
Gram matrices
Titanium
Multiscale

ABSTRACT

We present a methodology for the generative reconstruction of 3D microstructures from 2D cross-sectional electron backscatter diffraction micrographs. The method is applied to Ti-6Al-4V processed by laser powder bed fusion, where a high amount of basketweave morphology is observed, which arises from the solid-state $\beta \rightarrow \alpha$-transition upon cooling. Prior-$\beta$-grain reconstruction is performed and the out-of-plane orientation of the observed grains is obtained leveraging Burgers orientation relationship. Microstructural descriptors related to convolutional neural networks are extracted from the 2D micrographs, and used for cross-section-based optimization of pixel values in a 3D volume. In order to reconstruct crystallographic orientations, the orientation distribution of the basketweave microstructure is reduced to a discrete set of characteristic orientations, which are sequentially reconstructed as separate components. Our reconstructions capture the characteristic lath morphology that is typically observed in powder bed fusion-processed Ti-6Al-4V and perform well in comparisons of chord length, as well as grain size, aspect ratio, and axis orientation distributions.

## 1. Introduction

The macroscopic properties of any material are inherited from its microscopic characteristics. Due to the virtually infinite variety of microstructures occurring in engineering materials, numerical analysis of microstructures has become an essential tool to investigate the relationship between (micro)structure and property of a material. Acquisition of three-dimensional (3D) microstructural data is generally associated with high experimental effort, destructive procedures, or limited spatial resolution. Therefore, two-dimensional (2D) data is commonly used as a basis for numerical investigations. However, this dimensionality reduction introduces significant limitations, as it can result in imprecise predictions of material response [1] and fails to accurately capture physical phenomena such as the activation of slip systems [2] or fatigue mechanisms [3], which requires determination of the full 3D stress state at material points. Additionally, volumetric characteristics of the observed microstructure, like grain volumes or interconnectivity of microstructural features, are lost. To mitigate the aforementioned limitations, a representative 3D microstructural solution domain needs to be obtained.

Structure-property analyses of polycrystalline materials are commonly based on Electron Backscatter Diffraction (EBSD) micrographs, as they capture information about the material phase and crystallographic orientation at the observed points in the micrograph domain. However, unlike other techniques like Computer Tomography (CT), it cannot penetrate the material and needs to be performed on free surfaces. Therefore, the only way to experimentally obtain 3D EBSD data is the iterative removal of material, surface preparation, and data recording. Procedures for material removal include mechanical polishing [4–6], Focused Ion Beam (FIB) milling, [7–9] and laser ablation [10]. Limitations of these approaches are the time required to collect large datasets and the limited resolution normal to the serial sections.

An alternative is the synthetic generation of microstructures by geometrical construction algorithms like Voronoi tesselations [11] or equivalent ellipsoidal grain packing [12]. Due to the greatly reduced expense compared to the acquisition of 3D EBSD data through sequential slicing, it is a common choice for microstructures of low to moderate complexity. This approach has been applied successfully to study the elastoplastic response [13], damage [14], fatigue [15,16],

* Corresponding author.
*E-mail address:* v.m.blumer@utwente.nl (V. Blümer).

https://doi.org/10.1016/j.actamat.2025.120947
Received 22 November 2024; Received in revised form 12 February 2025; Accepted 16 March 2025
Available online 25 March 2025

and cracking [17,18] of microstructures predominantly composed of equiaxed, convex grains, with homogeneously spread properties across the observed domain. These are commonly observed in steels [13], Inconel [16], and Aluminum (Al) [19] among others. Heterogeneously distributed grain sizes [20] and preferential alignment of grains [21] can be obtained using Voronoi tessellations. However, the approach struggles to capture the characteristics of more intricate microstructures, including non-convex or intersecting grains. The ellipsoid grain placement algorithm is also subject to certain limitations, as it places grains only in largely unoccupied spaces, preventing the formation of intersecting grains. Additionally, some of the required microstructural properties like the neighbor distribution function can be difficult to extract when the observed grains vary significantly in size and aspect ratios, further complicating the use of the method for microstructure characterization and reconstruction. These limitations underscore the need for more versatile approaches that rely on minimal user-provided microstructural information and are capable of constructing grains with arbitrary shapes.

Titanium (Ti) alloys can occur in complex morphologies depending on their composition and thermal history, especially when processed by additive manufacturing [22,23]. The Laser Powder Bed Fusion (L-PBF) process, characterized by its rapid cooling and unique thermal conditions, invokes morphologies of fine grains and intricate substructures (see also Section 2), creating significant challenges for microstructural characterization and reconstruction methods. Recent studies highlight the importance of and difficulty associated with finding adequate microstructural representations for Ti-6Al-4V occurring in the form of basketweave morphology. Azhari et al. [24] generate two sets of microstructures based on either microstructural statistics or experimental serial sectioning of specimens fabricated by L-PBF. While the statistical microstructures show a similar homogenized elastoplastic response to those created from serial sectioning, the lath morphology is not captured. Somlo et al. [25] approximate the basketweave microstructure observed in L-PBF-processed Ti-6Al-4V as a laminate of alternating $\alpha$-Ti layers that have perpendicular orientations. With fitted material constants, the resulting stress–strain curves match experimental data well, but the approximation of the morphology is coarse. In similar fashion, Zhao et al. [26] resort to a combination of Voronoi tesselation and laminate structure to represent bimodal Ti-6Al-4V. Geng et al. [27] utilize a Voronoi tesselation with both homogeneous and lamellar grains with varying lath thicknesses to represent a similar microstructure observed in a functionally graded Ti-6Al-4V specimen manufactured by L-PBF. Liu et al. [28] emulate the observed microstructure in an L-PBF-manufactured Ti-6Al-4V specimen as an arrangement of simplistic geometrical elements over a 2D domain. Equipped with fitted mechanical constants, the experimental stress–strain curve is captured well. Zhang et al. [29] successfully quantify the effect of $\alpha/\beta$-interfaces in a forged Ti-7Mo-3Nb-3Cr-3Al alloy but are limited to 2D simulation domains due to the lack of accurate 3D representations of the microstructure.

In this work, we develop a methodology to reconstruct 3D microstructures from cross-sectional EBSD data that captures the characteristic lath microstructure, as well as distributions of grain aspect ratios, sizes, and axis orientations, when applied to Ti-6Al-4V basketweave morphology. We utilize and extend the MCRpy framework [30], which uses a pixel-value optimization through microstructural descriptors, to support the presented approach. Crystallographic orientation data is reconstructed through reduction of the observed orientation distribution to a discrete set of characteristic orientations, of which the associated grains are reconstructed sequentially. Our results in 2D and 3D demonstrate that the reconstructions capture both quantitative and qualitative characteristics of the Ti basketweave morphology.

The outline of the paper is as follows: In Section 2, we summarize the crystallography of Ti. Section 3 details the generative reconstruction of 3D data using an extended MCRpy implementation. Finally, Section 4 presents demonstration problems in both 2D and 3D.

## 2. Crystallography of Ti-6Al-4V

As a basis for subsequent sections, a brief introduction to the crystallographic properties of Ti-6Al-4V is given. An important property for the presented reconstruction approach is the Burgers orientation relationship (OR) between the $\alpha$ and $\beta$ phases in Ti. It benefits the reconstruction approach as it invokes an orientation distribution that is closely spread around twelve distinct angles.

### 2.1. Phases and transformations

At high temperatures, Ti occurs in body-centered-cubic (bcc) $\beta$ phase. When cooled across the $\beta$ transus temperature, it transforms into hexagonal-closest-packed (hcp) $\alpha$ phase. The most commonly observed morhologies depending on the thermomechanical processing route are equiaxed $\alpha$, lamellar $\alpha$+$\beta$ (Widmannstätten, basketweave), martensitic $\alpha'$, or bi-modal, comprised of equiaxed $\alpha$ embedded in regions of lamellae [23]. Cooling from above the $\beta$ transus temperature typically leads to lamellar or martensitic microstructure. At low cooling of 1.5–20 °C/s, $\alpha$ plates nucleate and grow from the $\beta$ grain boundaries, creating a Widmannstätten microstructure, where coplanar grains are stacked in colonies [31]. At higher cooling rates up to 410 °C/s, $\alpha/\alpha'$ plates nucleate also in the interior of $\beta$ grains, forming a basketweave morphology, where grains intersect at recurring angles [31]. Cooling rates exceeding 410 °C/s create a fully martensitic $\alpha'$ microstructure [22]. Equiaxed $\alpha$ is obtained by cooling from below the $\beta$ transus temperature [23] or very slow cooling from above the $\beta$ transus temperature [31]. Martensite is formed by the supersaturation of V in the $\alpha$ phase and occurs in the form of distorted-hcp $\alpha'$ at local concentrations of $< 10$ at.% V and orthorhombic $\alpha''$-martensite at local concentrations of $> 10$ at.% V [32]. The latter is not commonly observed in Ti-6Al-4V.

In Ti alloys, $\alpha$ and $\beta$ phases maintain the Burgers OR, specifically the alignment of $\{110\}_\beta \parallel \{0001\}_\alpha$ plane normals and $\langle 111\rangle_\beta \parallel \langle 11\bar{2}0\rangle_\alpha$ directions [33,34]. As a result, there are twelve variants of $\alpha$ grains within a single parent $\beta$ grain. $\alpha$ plates nucleate and grow along preferred crystallographic directions, resulting in the formation of plates oriented within specific planes, referred to as habit planes [35,36]. In basketweave formation, all twelve variants of the $\beta$ to $\alpha$ transformation can be observed, leading to the characteristic, intersecting grain morphology. In Widmannstätten colonies, regions of stacked $\alpha$-plates form with identical habit plane normal and crystallographic alignment, originating from the same $\beta$ grain [37].

### 2.2. Microstructural evolution during Laser Powder Bed Fusion (L-PBF)

The L-PBF process is characterized by rapid, repeated heating and subsequent cooling [38]. The molten powder solidifies as $\beta$ Ti in columnar grains that extend along the build direction, due to the highly directional temperature gradient during the process [34]. Among these grains, the preferred crystal orientation is the alignment of the $[001]_\beta$-direction with the build direction. In the proximity of free surfaces of a printed part, prior $\beta$ grains tend to be inclined towards the build direction and have weaker texture [39].

Upon cooling past the $\beta$ transus temperature, the $\beta$ Ti transforms into $\alpha/\alpha'$ phase, where, depending on process parameters and location in the specific build geometry, $\alpha'$ martensite is typically the dominant phase [40]. However, $\alpha' \rightarrow \alpha + \beta$ decomposition is known to occur in-situ during the thermal cycling caused by the deposition of subsequent layers [40]. $\alpha + \beta$ microstructure is dominant in annealed L-PBF specimens [34], as well as specimens fabricated by Electron-Beam-PBF, as the substrate is kept at a higher temperature and printing is conducted in vacuum instead of inert gas [41]. The volume fraction of $\beta$ phase in regions of dominant $\alpha'$ is very low ($< 5\%$), while in regions of decomposed $\alpha + \beta$, it can be in the order of 10% [34]. Specimens consisting of $\alpha'$ martensite show higher ultimate strength, while those possessing $\alpha + \beta$ microstructure have higher ductility [40].

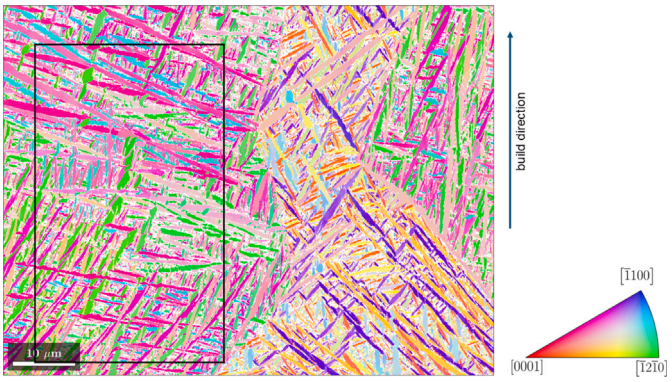


**Fig. 1.** EBSD micrograph of an LPBF-manufactured specimen built from Ti-6Al-4V alloy. The vertical axis is aligned with the build direction. The rectangular region is cropped out for further analysis.

The observed morphological arrangement of $\alpha/\alpha'$ grains in as-built L-PBF specimens is typically basketweave, as cooling rates are sufficiently high to allow nucleation of $\alpha/\alpha'$ grains in the interior of $\beta$ grains. Colonies of parallel Widmannstätten lamellae can be observed in regions of the print geometry with a deviating thermal history [37].

## 3. Generative reconstruction of 3D data

A flexible and robust approach to microstructure reconstruction is optimizing scalar pixel values in a reconstruction domain based on microstructural descriptors [30]. This process is the core of the powerful open-source platform MCRpy. To reconstruct a microstructure, a loss function is minimized, which is the difference between one or more descriptors computed over a target- and the reconstructed microstructure. The descriptor can be any expression computed over a microstructural image, like $n$-point statistics, total variation, or Gram matrices.

Depending on the choice of descriptors, the loss is a differentiable expression of all pixel values, meaning its partial derivatives w.r.t all pixel values in the reconstruction domain can be identified. Within a sufficiently small step from the current state, a change of the pixel values along their gradients is guaranteed to decrease the loss, and therefore, increase the resemblance of the target- and reconstruction domains.

In this contribution, we show that the reduction of the orientation distribution into a number of discrete orientations and sequential reconstruction is a robust approach to obtaining 3D microstructures of Ti basketweave, which is dominated by twelve characteristic orientations.

### 3.1. Acquired data

The generative 3D reconstruction procedure is applied to the microstructure observed in an EBSD micrograph of a Ti-6Al-4V specimen, which was manufactured using an Additive Industries MetalFAB1 printer. The process was conducted using a laser power of 375 W, a hatch spacing of 122 μm, and a layer thickness of 60 μm. These parameters were selected for experimental purposes and do not necessarily correspond to the optimal processing conditions for this machine. The micrograph shown in Fig. 1 is acquired using a JEOL JSM-7200F Scanning Electron Microscope (SEM), equipped with an Oxford Instruments Nordlys Nano EBSD detector. The physical dimensions of the micrograph are 77.86 μm × 58.09 μm and the resolution is 1072 × 800 pixels.

Basketweave microstructure can be observed everywhere in the micrograph. The separation of the region into elongated parent grains is directly apparent. The alignment convention of the crystal reference frame is $\boldsymbol{X} \parallel \boldsymbol{a}^*$, $\boldsymbol{Y} \parallel \boldsymbol{b}$, $\boldsymbol{Z} \parallel \boldsymbol{c}^*$, where $\boldsymbol{X}, \boldsymbol{Y}, \boldsymbol{Z}$ are the orthogonal axes

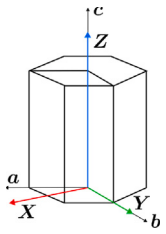


$$\begin{aligned} \boldsymbol{a}^* &= 2\pi \frac{\boldsymbol{b} \times \boldsymbol{c}}{\boldsymbol{a} \cdot (\boldsymbol{b} \times \boldsymbol{c})} \\ \boldsymbol{b}^* &= 2\pi \frac{\boldsymbol{c} \times \boldsymbol{a}}{\boldsymbol{a} \cdot (\boldsymbol{b} \times \boldsymbol{c})} \\ \boldsymbol{c}^* &= 2\pi \frac{\boldsymbol{a} \times \boldsymbol{b}}{\boldsymbol{a} \cdot (\boldsymbol{b} \times \boldsymbol{c})} \end{aligned} \tag{1}$$

**Fig. 2.** Relation of reference coordinate system $\boldsymbol{X}, \boldsymbol{Y}, \boldsymbol{Z}$ to crystal coordinate system $\boldsymbol{a}, \boldsymbol{b}, \boldsymbol{c}$ and expressions for the computation of reciprocal crystal axes $\boldsymbol{a}^*, \boldsymbol{b}^*, \boldsymbol{c}^*$, where $\cdot$ denotes the dot product and $\times$ the cross product between two vectors. A reciprocal crystal axis is orthogonal to both other crystal axes so that $\bullet^* \cdot \circ = 0$ and $\bullet^* \cdot \bullet = 2\pi$ where $\bullet, \circ \in \{\boldsymbol{a}, \boldsymbol{b}, \boldsymbol{c}\}$ and $\bullet \neq \circ$.

of the reference coordinate system and $\boldsymbol{a}, \boldsymbol{b}, \boldsymbol{c}$ are the crystal axes of the hcp lattice, where $\boldsymbol{a}$ and $\boldsymbol{b}$ are inclined at a 120° angle, as shown in Fig. 2.

### 3.2. Parent grain reconstruction

As Ti undergoes $\beta \rightarrow \alpha$-transformation, the emerging $\alpha$ grains have one of twelve relative orientations to the parent $\beta$-grain's orientation. The full set of possible alignments of the $\alpha$-crystals axes $\boldsymbol{X}_\alpha[\bar{1}100]$, $\boldsymbol{Y}_\alpha[11\bar{2}0]$, $\boldsymbol{Z}_\alpha(0001)$ to the parent $\beta$-grain lattice can be extracted from Furuhara et al. [42]. The emerging grains grow in the plane with the $\boldsymbol{Y}_\alpha[11\bar{2}0]$ normal direction, which is referred to as the habit plane [36]. This leads to the characteristic basketweave appearance of the grains in micrographs, as the habit plane intersects the observation plane.

Parent grain reconstruction is performed using the crystallographic analysis library MTEX [43,44]. In this process, the orientations of $\alpha$-grains are evaluated to reconstruct the orientations of a region's parent grain and the associated orientation variant of each $\alpha$-grain. Fig. 3 shows the reconstructed orientation of each $\alpha$-grain's parent grain.

In order to create a microstructure that exclusively contains the basketweave pattern emerging from one prior $\beta$ grain, the rectangular region shown in Fig. 1 is used for further analysis. Fig. 4 shows the computed orientation variants of the $\alpha$ grains. All grains that belong to one of the misorientation variants (hereafter called grain group) have almost identical grain axis orientations in the 2D observation plane, in addition to their identical crystal lattice orientations. The preferred growth plane of an $\alpha$-grain is called the habit plane, which is normal to one of the families of $[1100]_\alpha$-directions of the $\alpha$-crystal after transformation [45]. Therefore, the grain axis orientation in the out-of-plane dimension can be reconstructed, except for the ambiguity caused by the symmetry of the crystal lattice.

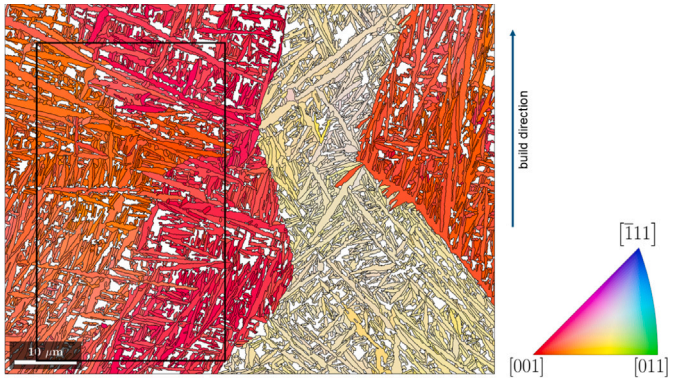


**Fig. 3.** Computed orientations of parent grains after prior $\beta$ grain reconstruction is performed in MTEX.

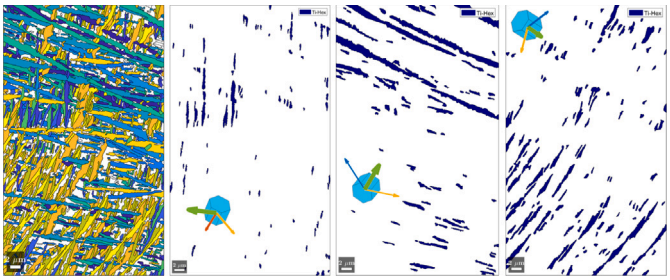

**Fig. 4.** During the prior $\beta$ grain reconstruction, each $\alpha$ grain is matched to one of the twelve variants of Burgers OR. All $\alpha$-grain groups are extracted from the EBSD, and their habit plane normals are computed. The green vector shows the matched habit plane normal. This process is shown for three of the twelve groups.

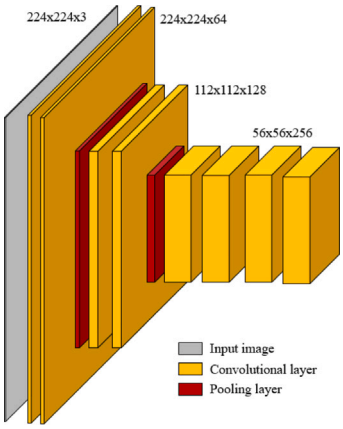


**Fig. 5.** Visualization of the truncated VGG-19 model that is used in MCRpy. Image dimensions are given as $J = K = 224$, as this is the resolution that the network is trained with. It can be applied to images with arbitrary resolution.

Due to the hcp-lattice's rotational symmetry around the $z$-axis, applying Burgers OR yields three vectors that potentially represent a grain group's habit plane normal. These vectors are projected onto the observation plane and compared against the in-plane grain axis. The vector that is closest to orthogonal to the grain axis is selected as the most plausible habit plane normal. Results of this process are shown in Fig. 4. The habit plane normals are later used to assemble the microstructural descriptors in orientations consistent with the 3D orientations of grains (see Section 3.6).

### 3.3. Microstructural descriptors

A microstructural descriptor is a metric that can be computed over a 2D image and contains quantitative information about the image's characteristics. Low-dimensional microstructure descriptors are volume fractions and grain size distributions, among others. More recently, Gram matrices [46] have emerged as a powerful, albeit intransparent descriptor for an image's overall characteristics. Despite their lack of interpretability, they have been used effectively to reconstruct micrographs [47]. MCRpy offers a selection of different descriptors that can be used individually or as a weighted sum to quantify the similarity between two compared microstructures.

Gram matrices are calculated from the activations of a pre-trained Convolutional Neural Network (CNN) when exposed to an image. CNNs are a class of neural networks that are commonly used for image recognition. They typically consist of a number of convolutional and pooling layers for visual feature extraction, shown in Fig. 5, and fully connected layers for image classification. A CNN is trained by optimization of model parameters (e.g. kernel weights and biases) in the convolutional layers during repeated exposure to a large set of images and corresponding ground truth labels. After the information is processed by the network's layers (forward propagation), the computed output probabilities are compared to the labels using a loss function. Partial derivatives of the loss w.r.t all model parameters are calculated (backpropagation) and the parameters are updated using an optimization scheme to obtain a network with gradually increased performance at classification of the images. This process is repeated until the optimizer reaches its convergence criterion [48]. One of the most well-established CNNs for general image recognition is the VGG-19 model [49]. MCRpy utilizes a truncated form of VGG-19 with pre-trained ImageNet weights [30]. Note that kernel weights are not subject to further optimization during image reconstruction with MCRpy.

In convolutional layers, a set of kernels (or filters) operate on an input layer of size $J \times K \times L$ to compute an output layer. Kernels are most commonly of dimensions $3 \times 3 \times L$, where $L$ is the depth of the previous layer. In the convolution operation, the kernel is moved across the input layer in steps of two pixels at a time. At each position, the scalar product of the kernel with the $3 \times 3 \times L$ part of the input layer at that position is taken. This procedure returns a feature map ($J \times K \times 1$) when computed for the full input layer. The convolution operation is carried out with all $N$ kernels, assembling the full output layer, which is a stack of feature maps ($J \times K \times N$). The depth of the output layer equals the number of kernels $N$ and is not necessarily equal to the depth of the input layer $L$.

In pooling layers, the output layer contains the average or maximum value of every $2 \times 2$ region in the input layer, which halves the dimensions $J$ and $K$ and increases the receptive field of subsequent layers.

For calculating the Gram matrix of layer $i$, the feature maps are flattened into vectorized feature maps of size $J\,K \times 1$. The stack of vectorized feature maps $F_{ij}$ is a matrix of shape $J\,K \times N$. The Gram matrix $G_{ij}$ is computed by taking the inner product of a stack of vectorized feature maps with its transpose, or

$$G^i_{pg} = \sum_r F^i_{pr} F^i_{qr} \tag{2}$$

in indicial notation [46]. The loss of a layer $i$ is the sum of the squared differences between entries in the Gram matrix of the target image $G_{ij}$ and reconstruction image $\widetilde{G}_{ij}$

$$\mathcal{L}^{\mathcal{G}}_i = \frac{1}{4N_i^2 M_i^2} \sum_{j,k} \left( G^i_{jk} - \widetilde{G}^i_{jk} \right)^2 , \tag{3}$$

where $N_i$ is the number and $M_i = J_i K_i$ the size of feature maps in layer $i$ [46]. The Gram matrix loss $\mathcal{L}^{\mathcal{G}}$ is the sum of losses

$$\mathcal{L}^{\mathcal{G}} = \sum_i \mathcal{L}^{\mathcal{G}}_i \tag{4}$$

over all layers i.

The total loss $\mathcal{L}$ of a 2D microstructure is a weighted sum of loss contributions from all selected descriptors

$$\mathcal{L}_{2D} = \sum_i^{n^{\text{des}}} \lambda^{\text{des}}_i \mathcal{L}^{\text{des}}_i . \tag{5}$$

The morphological characterization and reconstruction of microstructures in this work relies solely on the contribution from Gram matrices to the loss function $\mathcal{L}^{\mathcal{G}}$, while image noise is moderated through contribution of the normalized total variation $\mathcal{L}^{\mathcal{V}}$ and accuracy of reconstructed volume fractions is improved through the contribution of volume fractions $\mathcal{L}^{\phi}$. In 3D, the loss is accumulated over all slices of

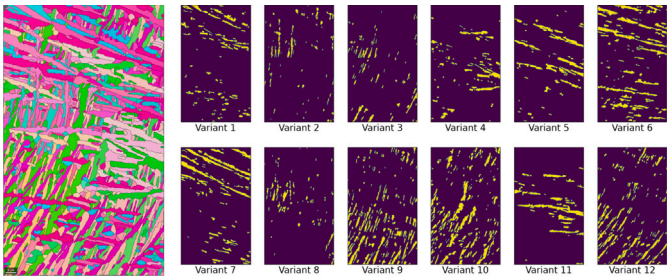


**Fig. 6.** Decomposition of the base data into twelve separate systems and reduction from orientation data to variant identifier numbers. More details of the encoding can be extracted from Table 1.

the microstructure in the orthogonal planes [50]

$$\begin{aligned}\mathcal{L}_{3D} = &\sum_{j}^{n_x^{\text{slices}}}\sum_{i}^{n^{\text{des}}} \lambda_i^{\text{des}} \mathcal{L}_i^{\text{des},j} + \\ &+ \sum_{k}^{n_y^{\text{slices}}}\sum_{i}^{n^{\text{des}}} \lambda_i^{\text{des}} \mathcal{L}_i^{\text{des},k} + \\ &+ \sum_{l}^{n_z^{\text{slices}}}\sum_{i}^{n^{\text{des}}} \lambda_i^{\text{des}} \mathcal{L}_i^{\text{des},l} \,.\end{aligned} \tag{6}$$

Assigning different targets to the descriptors on individual planes allows to introduce anisotropy into the reconstructed 3D microstructures. Descriptor weights are generally kept constant across all planes.

### 3.4. Extension of the MCRpy implementation

MCRpy is primarily built for the reconstruction of binary microstructures by varying pixel values in a continuous range from zero to one and does not readily support the reconstruction of orientation data. A way to circumvent this limitation is to encode the orientation distribution into a moderate number of discrete, characteristic orientations, which are represented as separate components in the context of MCRpy. The reconstruction of multi-component microstructures is supported by the MCRpy base implementation, but the addition of a third component already leads to a substantial increase in computational time. Reconstructions of the order of ten components are infeasible. The proposed approach is to decompose the multi-component reconstruction into separate binary systems where each component is reconstructed against a background of empty space. The resulting microstructures are superposed to arrive at a reconstruction of the full multi-component problem.

To proceed with this approach, a number of changes need to be introduced in the MCRpy implementation. Most importantly, it needs to be ensured that the separated reconstructions do not occupy the same regions in the reconstruction domain, as this would lead to a change in material volume fraction and other characteristics during the superposition of the separate components.

This is done by tracking the available space throughout the reconstructions. After reconstruction of one component, the occupied pixels are recorded and initialized as zero for all following reconstruction processes. The gradient computation is also modified so that all inactive pixels are assigned a constant gradient of zero and are thereby excluded from the optimization. The implemented modifications are compatible with MCRpy's multigrid procedure, which utilizes stepwise upsampling of the reconstruction domain resolution to decrease computational time.

The choice of an appropriate tolerance for the termination of the optimization is also necessary to ensure feasible runtimes. The L-BFGS method is used to drive the optimization, where the specified tolerance TOL is compared against

$$\frac{\mathcal{L}^k - \mathcal{L}^{k+1}}{\max\left(|\mathcal{L}^k|, |\mathcal{L}^{k+1}|\right)} \leq \texttt{TOL}\,. \tag{7}$$

All reconstructions in this work are computed using $\texttt{TOL} = 10^{-3}$.

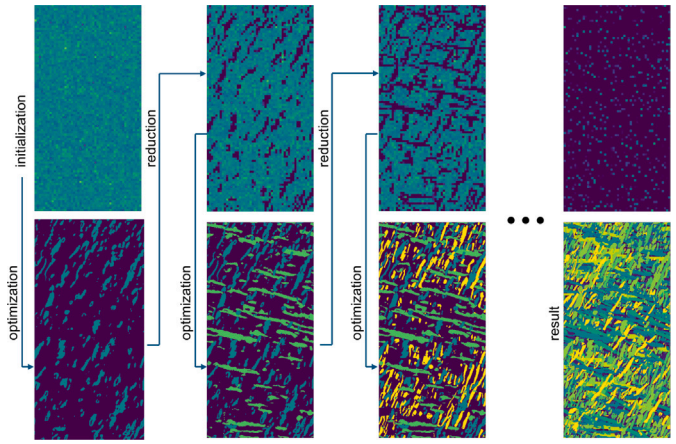


**Fig. 7.** The sequential reconstruction process is depicted for the first three and last variants in columns from left to right. The top row shows the initialized reconstruction domain of each process and the bottom rows shows superposed results. The first process is initialized with random noise. In each subsequent process, all points utilized by a previous reconstruction are initialized as zero, deactivating them from the current reconstruction. The domains in the top row have one-eighth of the resolution as the finished reconstruction domains due to the use of the multigrid scheme in MCRpy.

**Table 1**
Assignment of characteristic orientations to variant identifiers and their respective Volume Fractions (VF) and Inverse Pole Figure (IPF) colors in Fig. 6.

| Variant | Orientation $(\varphi_1, \Phi, \varphi_2)$ [°] | | | Habit plane normal | | | VF [%] | IPF |
|---|---|---|---|---|---|---|---|---|
| 1 | 104.62 | 88.36 | 45.73 | 0.008 | −0.290 | 0.957 | 6.696 | |
| 2 | 157.14 | 47.14 | 22.47 | −0.946 | 0.109 | 0.304 | 3.635 | |
| 3 | 65.81 | 33.96 | 18.48 | −0.627 | 0.518 | 0.582 | 4.086 | |
| 4 | 104.34 | 88.31 | 58.04 | −0.188 | 0.501 | 0.845 | 5.678 | |
| 5 | 154.50 | 49.11 | 16.09 | −0.516 | −0.472 | 0.714 | 7.445 | |
| 6 | 63.76 | 37.79 | 29.43 | 0.026 | 0.952 | 0.306 | 13.951 | |
| 7 | 142.50 | 139.47 | 24.90 | 0.376 | 0.633 | 0.677 | 10.347 | |
| 8 | 14.65 | 83.05 | 7.05 | −0.647 | −0.054 | 0.761 | 3.442 | |
| 9 | 142.55 | 139.76 | 13.34 | 0.864 | 0.005 | 0.504 | 12.765 | |
| 10 | 14.94 | 80.09 | 60.20 | −0.495 | 0.010 | 0.869 | 14.139 | |
| 11 | 55.66 | 128.37 | 19.03 | 0.693 | 0.658 | 0.294 | 6.778 | |
| 12 | 58.80 | 124.49 | 32.65 | 0.485 | −0.344 | 0.804 | 10.619 | |

### 3.5. Reconstruction process

In preparation for the reconstruction process, grains are reconstructed from the base EBSD data (Fig. 1) in MTEX. Computed grains of area $< 0.1\ \mu m^2$ are considered artifacts and removed from the data to simplify the obtained grain morphology (Fig. 3). All non-indexed points in the base data are filled with the value of their nearest neighbor inside their computed grains to minimize the amount of empty space in the target microstructure for the reconstruction process (Fig. 6). This step leaves parts of the data points in the corner- and edge locations of the EBSD non-indexed, which explains why the volume fractions of the target microstructure in Tables 2 and 3 do not sum to 100%. Next, the base data is transformed from a single domain that contains orientation data into twelve separate maps that contain binary data, where each characteristic grain orientation in the base data is encoded into a variant identifier number. Fig. 6 shows the decomposition of the image into separate reconstruction problems.

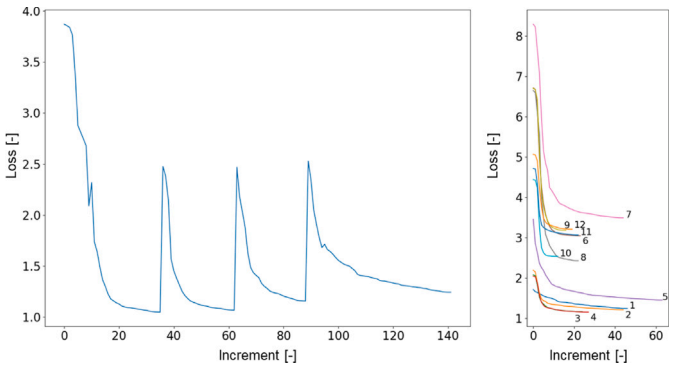


**Fig. 8.** Left: For the first of the twelve sequential reconstructions, the loss at each iteration of the optimization is shown. Each doubling of the resolution causes a jump in the loss. The reconstruction domain is initialized as $50 \times 81$ pixels and upsampled whenever TOL of $10^{-3}$ is met until the full resolution of $400 \times 650$ is reached. Right: For all twelve reconstructions, the loss at each iteration of the full-resolution stage is shown. Increments are counted relative to the start of the full-resolution stage of each respective reconstruction process. Earlier reconstructions can reach lower loss values as more space in the reconstruction domain is available.

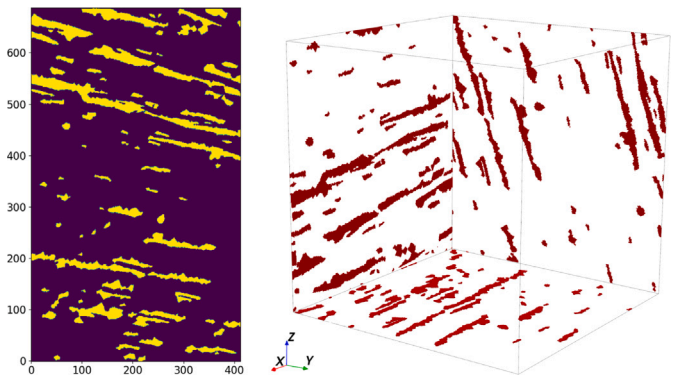

**Fig. 9.** Three-dimensional assembly of target domains shown for the 6th variant. It is assumed that the morphological pattern captured in the EBSD data represents the observed grain group reasonably well on orthogonal planes. The grain pattern of variant 6 is rotated to align with the computed habit plane normal of $(0.03, 0.95, 0.31)$.

Table 1 shows the encoding of characteristic orientations into variant identifier numbers. Habit plane normals are calculated using Burgers OR as outlined in Section 3.2. Volume fractions are calculated from the filled EBSD data.

The variants are reconstructed in the order of decreasing volume fraction. The reconstruction domain for the first reconstruction is initialized as normally distributed values around 0.5 with a standard deviation of 0.1 and min- and max-cutoff at 0.1 and 0.9 (see Fig. 7, top left). Pixel values in the reconstruction domain are optimized to minimize the loss, which is computed from the selected descriptors. Once the specified tolerance is reached, a Gaussian filter is applied to the reconstructed microstructure to further reduce noise [30], which concludes the reconstruction of one variant (Fig. 7, bottom left). This procedure is repeated for all variants, during which the occupied space is tracked and removed from the initializations of later reconstructions (Fig. 7, top row).

Fig. 8 shows the loss throughout the reconstruction as defined in Eq. (5). To save computational time, the reconstruction domain is initialized as $50 \times 100$ and upsampled multiple times until the full resolution of $400 \times 800$ is reached. Each upsampling is associated with a jump in the loss as the resolution of the descriptor and reconstruction domain doubles. Fig. 8 also shows the convergence of the loss in the final stage of the optimization for all variants. As the available space for reconstruction decreases throughout the process, losses for later reconstructions tend to converge at higher values than earlier ones. The resulting effects are decreased by reconstructing variants to decrease the variant fraction.

Once all reconstruction processes are completed, the resulting microstructures can be superposed without intersection. The variant identifiers are decoded back into Euler angles, which allows for direct comparison to the EBSD target data. The approach in its current form is limited to the reconstruction of the substructure within one prior $\beta$ grain. This is because no information on relative spatial (co-)occurrence in between the variants is conveyed, which is required for the substructures within each $\beta$ grain not to blend in the reconstruction. In the context of computational mechanics, investigation of larger regions spanning across a multitude of prior $\beta$ grains with distinct orientations and variant selections require the use of effective properties in a multiscale approach.

### 3.6. Out-of-plane descriptors

In the case of 3D microstructure reconstructions, appropriate descriptors for all three orthogonal planes need to be obtained. This can be done through additional EBSD micrographs or morphological assumptions, if the investigated material allows. As for the case of the Ti basketweave microstructure, the habit plane of each grain can be extracted from Burgers OR, which identifies the grain's out-of-plane axis orientation. For the 3D reconstruction of a grain group, the cross-sections of its habit plane and the orthogonal descriptor planes are computed. As for the lack of available 3D data, it is assumed that the grain morphology observed in the EBSD observation plane is representative of all orthogonal planes. Micrographs taken on different planes reveal that the morphology of the $\alpha$ grain patterns itself remains largely insensitive to the build direction in L-PBF manufacturing, while the effect of the highly directional temperature gradient are predominantly seen in the morphology of prior $\beta$ grains [51]. To construct the out-of-plane descriptors, the grain pattern observed in the EBSD is rotated to the computed angle at which the habit plane and the respective descriptor plane intersect. The resulting assembled target domains are visualized in Fig. 9.

## 4. Results

The proposed methodology is utilized to create reconstructions of the basketweave pattern observed in the EBSD micrograph (Fig. 1). We present results for a 2D reconstruction of size $400 \times 650$ in Section 4.1, and results for a 3D reconstruction of size $200 \times 200 \times 200$

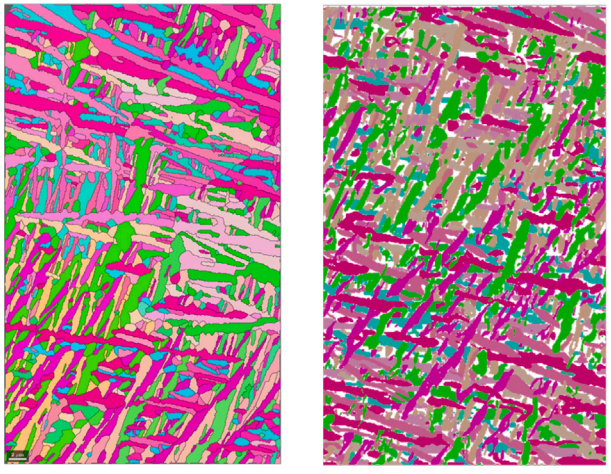

**Fig. 10.** Left: Target 2D microstructure ($413 \times 688$) before decomposition, as seen in Fig. 6. Right: Reconstructed 2D microstructure ($400 \times 650$).

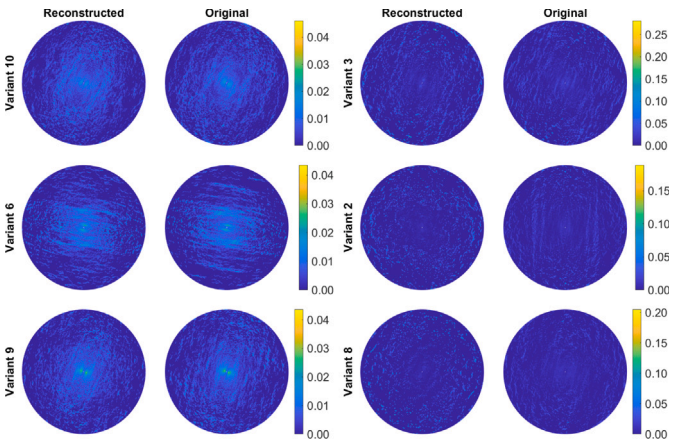


**Fig. 11.** Chord length distribution in the 2D target and reconstructed microstructures. Results are shown for the first (left) and last (right) three variants in order of decreasing volume fraction.

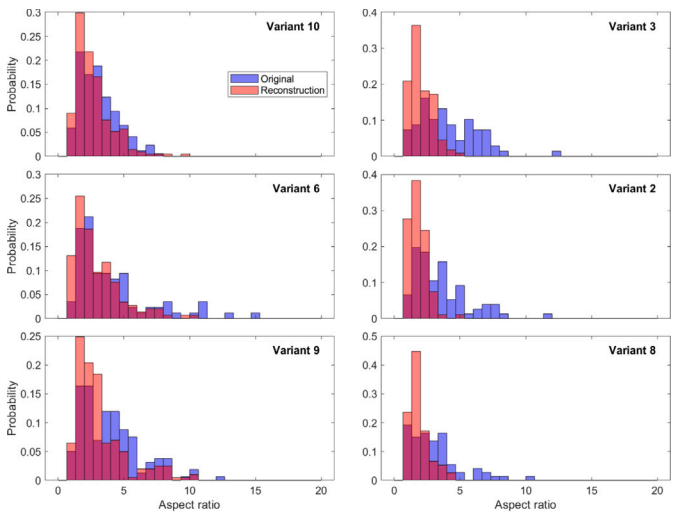


**Fig. 12.** Distribution of grain aspect ratios in the 2D target and reconstructed 2D microstructures. Results are shown for the first (left) and last (right) three variants in order of decreasing volume fraction.

in Section 4.2. Geometrical quantification is based on comparisons of grain aspect ratio-, grain axis-, and grain size distributions as well as chord length distributions (CLD). For the purpose of brevity, only a representative subset of the computed data is presented in the following sections. For the full set of results, the reader is referred to the supplementary materials.

### 4.1. 2D reconstruction

The resolution of 400 × 650 is selected for the reconstruction of the 2D microstructure to approximately match that of the target microstructure taken from the EBSD data (413 × 688). Relative descriptor weights of $\lambda_G = 1$ for Gram matrices and $\lambda_V = \lambda_{VF} = 100$ for volume fraction and variation are used. As seen in Fig. 10, the reconstructed microstructure shows strong qualitative similarity to the EBSD base data and captures key characteristics like high aspect ratio, intersecting grains, and characteristic grain orientations. The reconstruction domain is not filled with material after the reconstruction process has concluded. To fill the remaining space, the suggested approach is to assign the empty points the data from the nearest neighboring grain, as is done with the non-indexed points in the EBSD data in Section 3.5.

Fig. 11 shows the angularly resolved CLDs of the first and last three variants in order of their reconstruction, computed using the implementation provided by Latypov et al. [52]. Results of all variants are given in the supplementary materials. The CLD captures the distances between intersections of test lines at a given angle with grain boundaries of a microstructure. The CLD for each angle of test lines from $[0°, 180°]$ is computed, and the resulting histograms are represented at their respective angle in circular fashion, as seen in Fig. 11. From the CLDs, it can be concluded that all but the last two variants show a good match of preferred grain axis orientations. The preferred grain orientation among grains belonging to the same variant is one of the most characteristic properties of the target microstructure and is captured remarkably well, given that the descriptor is not provided with any explicit information regarding this property.

Fig. 12 shows the distribution of grain aspect ratios of the first and last three variants in order of reconstruction. Aspect ratios are computed as the ratios of long over short axes of ellipses that are fitted to grains [53]. The match of the first three distributions is good, and a reliable occurrence of grains with aspect ratios > 5 can be observed, which is characteristic of the target microstructure. The last three reconstructions are increasingly burdened by the lack of available space and show more significant differences when compared to the target data, though the match of trend and order of magnitude is still fair.

**Table 2**
Required iterations, computational time, and volume fractions of the 2D reconstructions in order of their computation. Volume fraction of the binarized optimization result is denoted by $\phi_{opt}$, volume fraction after application of the Gaussian filter, which is the final product of the reconstruction process, is denoted by $\phi_{rec}$.

| Variant | Iterations | Time [min] | $\phi_{target}$ [%] | $\phi_{opt}$ [%] | $\phi_{rec}$ [%] |
|---|---|---|---|---|---|
| 10 | 52 | 2.67 | 14.14 | 15.12 | 14.55 |
| 6 | 44 | 2.30 | 13.95 | 14.79 | 14.60 |
| 9 | 24 | 1.76 | 12.77 | 13.20 | 13.02 |
| 12 | 27 | 1.90 | 10.62 | 10.77 | 10.56 |
| 7 | 68 | 3.03 | 10.35 | 10.88 | 10.54 |
| 5 | 23 | 1.86 | 7.45 | 6.06 | 5.84 |
| 11 | 44 | 2.50 | 6.78 | 5.85 | 5.51 |
| 1 | 22 | 1.81 | 6.70 | 5.65 | 5.36 |
| 4 | 16 | 1.66 | 5.68 | 4.01 | 3.77 |
| 3 | 12 | 1.47 | 4.09 | 2.39 | 2.16 |
| 2 | 22 | 1.70 | 3.64 | 1.97 | 1.75 |
| 8 | 19 | 1.66 | 3.44 | 1.67 | 1.46 |
| Sum | 373 | 24.32 | 99.58 | 92.37 | 89.12 |

### 4.2. 3D reconstruction

A resolution of 200 × 200 × 200 is selected for the 3D reconstruction to limit the required computational effort. To circumvent the issue of resolution mismatch between the target and reconstruction domain, the target microstructure is downsampled from its original size to half its resolution and cropped to a square shape of 200 × 200 pixels. Relative descriptor weights of $\lambda_G = 1$ for Gram matrices and $\lambda_V = 100$ for variation are used.

Required iterations, computational time, and volume fraction of each reconstruction process can be extracted from Table 2. Reconstructed volume fractions are generally in good agreement with those of the base data, with slight over-representation in earlier reconstructions and under-representation in later stages.

As with the 2D reconstruction, the qualitative agreement to the base data is good and key characteristics are present in the reconstruction, as can be seen in Fig. 13. Required computational time, iterations, and volume fractions are presented in Table 3. Agreement of volume fractions of the reconstructed microstructure immediately after optimization is very good, the applied Gaussian filter however leads to a loss of material volume across all reconstructed variants. This decrease is more pronounced than in 2D reconstructions, because

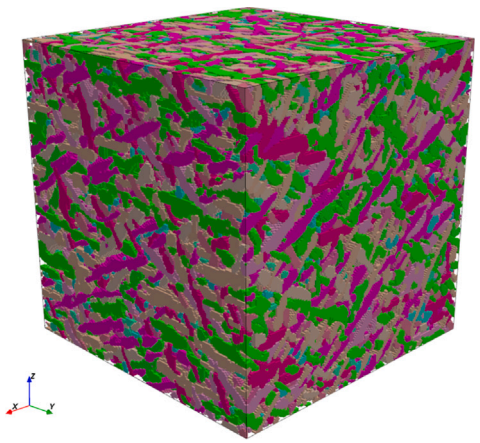

**Fig. 13.** Reconstructed 3D microstructure with a resolution of 200 × 200 × 200.

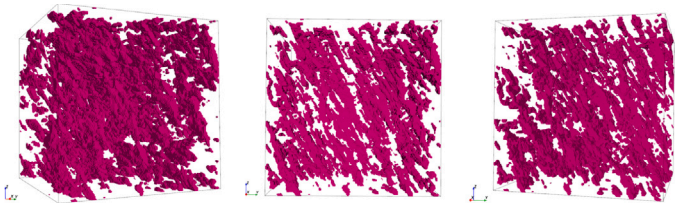

**Fig. 14.** Three slightly different views of an isolated variant visualize the out-of-plane morphology of the reconstructed grains. A qualitative resemblance to experimentally obtained data [7,54] is captured.

the level of noise is higher in 3D reconstructions, as also observed by Seibert er al. [50]. As compared to the 2D process, a shift in the order of reconstruction of individual variants occurs because the volume fraction of the target microstructures changes slightly during cropping.

Fig. 14 shows the morphology of a single reconstructed variant. For a visual comparison to experimentally obtained data, the reader is referred to results obtained by DeMott et al. [7] and Ma et al. [54]. A striking feature in both the experimental data as well as the reconstruction is the out-of-plane coherence of grains, which cannot be observed in 2D EBSD data.

Fig. 15 shows the angularly resolved CLDs as introduced by Latypov et al. [52] across the first and last three variants in order of reconstruction, extracted from five slices in $x$-direction. The resemblance of

**Table 3**
Required iterations, computational time, and volume fractions of the 3D reconstructions in order of their computation. Volume fraction of the binarized optimization result is denoted by $\phi_{opt}$, volume fraction after the application of the Gaussian filter, which is the final product of the reconstruction process, is denoted by $\phi_{rec}$. The sum of volume fractions of the optimization results can exceed 100%, as they are not required to be compatible as is the case with the reconstruction results.

| Variant | Iterations | Time [min] | $\phi_{target}$ [%] | $\phi_{opt}$ [%] | $\phi_{rec}$ [%] |
|---|---|---|---|---|---|
| 9 | 49 | 162.48 | 18.40 | 19.01 | 15.66 |
| 10 | 47 | 151.75 | 18.16 | 18.74 | 16.30 |
| 12 | 44 | 152.71 | 14.78 | 14.96 | 12.41 |
| 6 | 33 | 120.06 | 9.77 | 10.08 | 8.02 |
| 11 | 37 | 150.03 | 9.20 | 9.16 | 6.93 |
| 5 | 55 | 211.63 | 7.49 | 7.57 | 5.63 |
| 4 | 58 | 217.30 | 6.57 | 6.85 | 4.82 |
| 3 | 25 | 94.34 | 4.51 | 4.37 | 2.93 |
| 7 | 36 | 146.27 | 3.50 | 3.13 | 1.91 |
| 1 | 52 | 213.26 | 3.00 | 2.96 | 1.53 |
| 8 | 37 | 154.96 | 2.96 | 2.52 | 1.21 |
| 2 | 37 | 147.16 | 1.63 | 1.53 | 0.60 |
| Sum | 510 | 1921.95 | 99.97 | 100.90 | 77.95 |

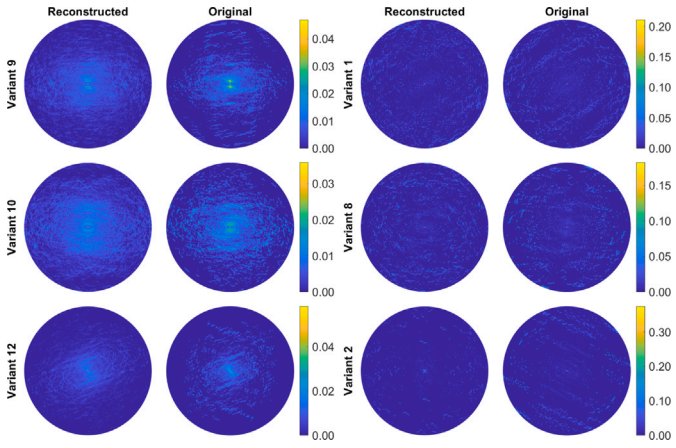


**Fig. 15.** Chord length distribution of five slices in $x$-direction extracted from the reconstructed 3D microstructure and corresponding data from the target microstructure. Results are shown for the first (left) and last (right) three variants in order of decreasing volume fraction.

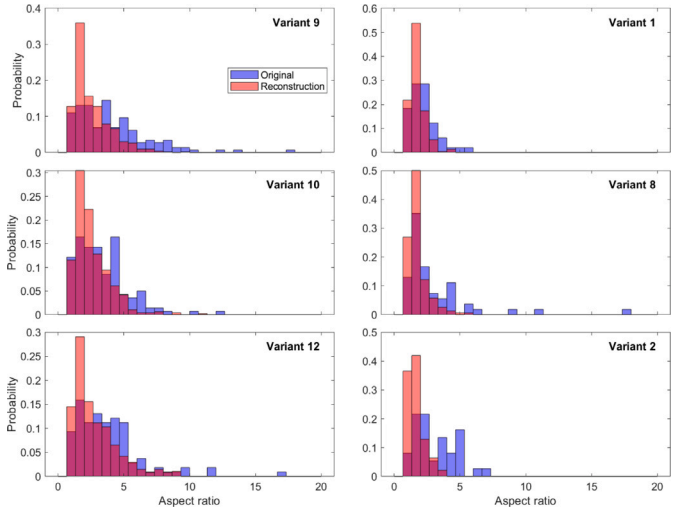


**Fig. 16.** Distribution of grain aspect ratios extracted from five slices in $x$-direction from the reconstructed 3D microstructure, and corresponding data in the target microstructure. Data is shown for the first (left) and last (right) three variants in order of reconstruction.

CLDs for the first three target- and reconstructed microstructures is good but not as striking as in the 2D reconstruction. This is presumably caused by the conflicting optimization targets on orthogonal planes of the structure. Same as with the 2D reconstructions, the last three reconstructions increasingly suffer from the lack of available space.

In Fig. 16, the distribution of grain aspect ratios across five slices in $x$-direction extracted from the reconstructed 3D microstructure is given. While the agreement of the first three reconstructions is fair, and the characteristic, reliable occurrence of sharp grains with aspect ratio > 5 is captured, results do not match as well as for the 2D reconstruction. This is presumably again caused by the conflicting optimization targets on orthogonal planes of the microstructure.

## 5. Conclusion

In this work, we present a robust methodology for the generative reconstruction of 3D microstructures that capture the basketweave mophology commonly observed in Ti-6Al-4V from 2D EBSD data. From our findings, we draw the following conclusions:

1. Reconstructions of Ti basketweave morphology can be obtained by reducing the orientation data obtained from EBSD micrographs to a multi-component reconstruction problem through encoding characteristic angles to identifier numbers. The resulting microstructures capture striking qualitative resemblance and show good quantitative agreement in several independent geometric comparison criteria.
2. The sequential treatment of the multi-component reconstruction problem allows its solution with feasible computational effort. The sequence in which reconstruction processes are conducted introduces increasingly strong constraints on latter reconstructions, but the resulting effects on the quality of the overall reconstruction are moderate.
3. Gram matrices perform well in capturing a blend of characteristics of the target microstructure, such as volume fractions as well as grain axis angles, grain aspect ratios, and grain sizes. Using total variation as an additional descriptor is needed to moderate image noise, especially in 3D reconstructions.

## CRediT authorship contribution statement

**Vincent Blümer:** Writing – review & editing, Writing – original draft, Visualization, Validation, Software, Methodology, Investigation, Formal analysis, Data curation, Conceptualization. **Ali Reza Safi:** Writing – review & editing, Visualization, Validation, Software. **Celal Soyarslan:** Writing – review & editing, Supervision, Project administration, Funding acquisition, Conceptualization. **Benjamin Klusemann:** Writing – review & editing, Supervision, Project administration. **Ton van den Boogaard:** Writing – review & editing, Supervision, Project administration, Funding acquisition.

## Declaration of competing interest

The authors declare that they have no known competing financial interests or personal relationships that could have appeared to influence the work reported in this publication.

## Acknowledgments

We would like to thank Sikander Naseem from the Fraunhofer Innovation Platform for Advanced Manufacturing at the University of Twente for supplying the EBSD micrographs. Benjamin Klusemann and Ali Reza Safi gratefully acknowledge funding from the European Research Council (ERC) under the European Unions Horizon 2020 research and innovation program (Grant Agreement No. 101001567).

## Data availability

The adapted MCRpy implementation is accessible as a fork of the original MCRpy GitHub repository [30] at https://github.com/vbluemer/MCRpy.

## References

[1] A. Ramazani, K. Mukherjee, H. Quade, U. Prahl, W. Bleck, Correlation between 2D and 3D flow curve modelling of DP steels using a microstructure-based RVE approach, Mater. Sci. Eng.: A 560 (2013) 129–139.
[2] F. Dunne, Fatigue crack nucleation: Mechanistic modelling across the length scales, Curr. Opin. Solid State Mater. Sci. 18 (4) (2014) 170–179.
[3] W.D. Musinski, D.L. McDowell, Microstructure-sensitive probabilistic modeling of HCF crack initiation and early crack growth in Ni-base superalloy IN100 notched components, Int. J. Fatigue 37 (2012) 41–53.
[4] S.-P. Tsai, P.J. Konijnenberg, I. Gonzalez, S. Hartke, T.A. Griffiths, M. Herbig, K. Kawano-Miyata, A. Taniyama, N. Sano, S. Zaefferer, Development of a new, fully automated system for electron backscatter diffraction (EBSD)-based large volume three-dimensional microstructure mapping using serial sectioning by mechanical polishing, and its application to the analysis of special boundaries in 316L stainless steel, Rev. Sci. Instrum. 93 (9) (2022).
[5] M.G. Chapman, M.N. Shah, S.P. Donegan, J.M. Scott, P.A. Shade, D. Menasche, M.D. Uchic, AFRL additive manufacturing modeling series: challenge 4, 3D reconstruction of an IN625 high-energy diffraction microscopy sample using multi-modal serial sectioning, Integr. Mater. Manuf. Innov. 10 (2021) 129–141.
[6] H. Sharma, S.M. Van Bohemen, R.H. Petrov, J. Sietsma, Three-dimensional analysis of microstructures in titanium, Acta Mater. 58 (7) (2010) 2399–2407.
[7] R. DeMott, P. Collins, C. Kong, X. Liao, S. Ringer, S. Primig, 3D electron backscatter diffraction study of $\alpha$ lath morphology in additively manufactured Ti-6Al-4V, Ultramicroscopy 218 (2020) 113073.
[8] R. DeMott, N. Haghdadi, Z. Gandomkar, X. Liao, S. Ringer, S. Primig, Formation and 3D morphology of interconnected $\alpha$ microstructures in additively manufactured Ti-6Al-4V, Materialia 20 (2021) 101201.
[9] J. Tiley, A. Shiveley, A. Pilchak, P. Shade, M. Groeber, 3D reconstruction of prior $\beta$ grains in friction stir–processed Ti–6Al–4V, J. Microsc. 255 (2) (2014) 71–77.
[10] M.P. Echlin, A. Mottura, C.J. Torbet, T.M. Pollock, A new TriBeam system for three-dimensional multimodal materials analysis, Rev. Sci. Instrum. 83 (2012) http://dx.doi.org/10.1063/1.3680111.
[11] S. Weyer, A. Fröhlich, H. Riesch-Oppermann, L. Cizelj, M. Kovac, Automatic finite element meshing of planar Voronoi tessellations, Eng. Fract. Mech. 69 (8) (2002) 945–958.
[12] M. Groeber, S. Ghosh, M.D. Uchic, D.M. Dimiduk, A framework for automated analysis and simulation of 3D polycrystalline microstructures. Part 2: Synthetic structure generation, Acta Mater. 56 (6) (2008) 1274–1287.
[13] M. Nygårds, P. Gudmundson, Three-dimensional periodic voronoi grain models and micromechanical FE-simulations of a two-phase steel, Comput. Mater. Sci. 24 (4) (2002) 513–519.
[14] T. Yu, H. Shi, Effects of grain size distribution on the creep damage evolution of polycrystalline materials, J. Phys. D: Appl. Phys. 43 (16) (2010) 165401.
[15] D. McDowell, F. Dunne, Microstructure-sensitive computational modeling of fatigue crack formation, Int. J. Fatigue 32 (9) (2010) 1521–1542.
[16] V. Prithivirajan, M.D. Sangid, The role of defects and critical pore size analysis in the fatigue response of additively manufactured IN718 via crystal plasticity, Mater. Des. 150 (2018) 139–153.
[17] P. Zhang, M. Karimpour, D. Balint, J. Lin, D. Farrugia, A controlled Poisson Voronoi tessellation for grain and cohesive boundary generation applied to crystal plasticity analysis, Comput. Mater. Sci. 64 (2012) 84–89.
[18] I. Simonovski, L. Cizelj, Cohesive zone modeling of intergranular cracking in polycrystalline aggregates, Nucl. Eng. Des. 283 (2015) 139–147.
[19] Z. Wang, P. Li, Voronoi cell finite element modelling of the intergranular fracture mechanism in polycrystalline alumina, Ceram. Int. 43 (9) (2017) 6967–6975.
[20] S. Biner, Thermo-elastic analysis of functionally graded materials using voronoi elements, Mater. Sci. Eng.: A 315 (1–2) (2001) 136–146.
[21] Z. Li, Z. Wu, A novel multiscale design method for porous structures with tunable anisotropy: Varied-shape Voronoi tessellation, Comput. Methods Appl. Mech. Engrg. 432 (2024) 117378.
[22] T. Ahmed, H. Rack, Phase transformations during cooling in $\alpha$+ $\beta$ titanium alloys, Mater. Sci. Eng.: A 243 (1–2) (1998) 206–211.
[23] A. Shaikh, S. Kumar, A. Dawari, S. Kirwai, A. Patil, R. Singh, Effect of temperature and cooling rates on the $\alpha$+ $\beta$ morphology of Ti-6Al-4V alloy, Procedia Struct. Integr. 14 (2019) 782–789.
[24] F. Azhari, W. Davids, H. Chen, S.P. Ringer, C. Wallbrink, Z. Sterjovski, B.R. Crawford, D. Agius, C.H. Wang, G. Schaffer, A comparison of statistically equivalent and realistic microstructural representative volume elements for crystal plasticity models, Integr. Mater. Manuf. Innov. 11 (2) (2022) 214–229.
[25] K. Somlo, K. Poulios, C.V. Funch, C.F. Niordson, Anisotropic tensile behaviour of additively manufactured Ti-6Al-4V simulated with crystal plasticity, Mech. Mater. 162 (2021) http://dx.doi.org/10.1016/j.mechmat.2021.104034.
[26] Y. Zhao, K. Tang, P. Ferro, F. Berto, Crystal plasticity modeling fatigue behavior in bimodal Ti-6Al-4V: Effects of microdefect and lamellar orientation, Fatigue Fract. Eng. Mater. Struct. 47 (2024) 2195–2214, http://dx.doi.org/10.1111/ffe.14292.
[27] Y. Geng, N. Harrison, Functionally graded bimodal Ti6Al4V fabricated by powder bed fusion additive manufacturing: Crystal plasticity finite element modelling, Mater. Sci. Eng. A 773 (2020) http://dx.doi.org/10.1016/j.msea.2019.138736.
[28] Y. Liu, F. Yu, Y. Wang, Mechanical anisotropy of selective laser melted Ti-6Al-4V using a reduced-order crystal plasticity finite element model, Chin. J. Mech. Eng.: Addit. Manuf. Front. 2 (2023) 100062, http://dx.doi.org/10.1016/j.cjmeam.2023.100062.
[29] M. Zhang, J. Li, B. Tang, W.Y. Wang, K. Li, T. Zhang, D. Wang, H. Kou, Quantification of $\alpha$ phase strengthening in titanium alloys: crystal plasticity model incorporating $\alpha/\beta$ heterointerfaces, Int. J. Plast. 158 (2022) 103444.
[30] P. Seibert, A. Raßloff, K. Kalina, M. Ambati, M. Kästner, Microstructure characterization and reconstruction in Python: MCRpy, Integr. Mater. Manuf. Innov. 11 (3) (2022) 450–466.
[31] R. Pederson, Microstructure and Phase Transformation of Ti-6Al-4V (Ph.D. thesis), Luleå Tekniska Universitet, 2002.
[32] W. Mei, J. Sun, Y. Wen, Martensitic transformation from $\beta$ to $\alpha'$ and $\alpha''$ phases in Ti-V alloys: A first-principles study, J. Mater. Res. 32 (16) (2017) 3183–3190.
[33] W. Burgers, On the process of transition of the cubic-body-centered modification into the hexagonal-close-packed modification of zirconium, Physica 1 (7–12) (1934) 561–586.

[34] C. Cepeda-Jiménez, F. Potenza, E. Magalini, V. Luchin, A. Molinari, M. Pérez-Prado, Effect of energy density on the microstructure and texture evolution of Ti-6Al-4V manufactured by laser powder bed fusion, Mater. Charact. 163 (2020) 110238.
[35] T. Furuhara, J. Howe, H. Aaronson, Interphase boundary structures of intragranular proeutectoid $\alpha$ plates in a hypoeutectoid Ti-Cr alloy, Acta Met. et Mater. 39 (11) (1991) 2873–2886.
[36] G. Lütjering, J.C. Williams, Titanium, Springer, 2007.
[37] K. Makiewicz, S. Babu, M. Keller, A. Chaudhary, Microstructure evolution during laser additive manufacturing of Ti6Al4V alloys, in: Proceedings of the International Conference, Trends Weld. Res. Chicago, IL, 2012.
[38] T. DebRoy, H.L. Wei, J.S. Zuback, T. Mukherjee, J.W. Elmer, J.O. Milewski, A.M. Beese, A.d. Wilson-Heid, A. De, W. Zhang, Additive manufacturing of metallic components–process, structure and properties, Prog. Mater. Sci. 92 (2018) 112–224.
[39] A.A. Antonysamy, J. Meyer, P. Prangnell, Effect of build geometry on the $\beta$-grain structure and texture in additive manufacture of Ti-6Al-4V by selective electron beam melting, Mater. Charact. 84 (2013) 153–168.
[40] W. Xu, M. Brandt, S. Sun, J. Elambasseril, Q. Liu, K. Latham, K. Xia, M. Qian, Additive manufacturing of strong and ductile Ti-6Al-4V by selective laser melting via in situ martensite decomposition, Acta Mater. 85 (2015) 74–84.
[41] X. Zhao, S. Li, M. Zhang, Y. Liu, T.B. Sercombe, S. Wang, Y. Hao, R. Yang, L.E. Murr, Comparison of the microstructures and mechanical properties of Ti-6Al-4V fabricated by selective laser melting and electron beam melting, Mater. Des. 95 (2016) 21–31.
[42] T. Furuhara, H. Nakamori, T. Maki, Crystallography of $\alpha$ phase precipitated on dislocations and deformation twin boundaries in a $\beta$ titanium alloy, Mater. Trans. JIM 33 (6) (1992) 585–595.
[43] F. Bachmann, R. Hielscher, H. Schaeben, Texture analysis with MTEX–free and open source software toolbox, Solid State Phenom. 160 (2010) 63–68.
[44] F. Niessen, T. Nyyssönen, A.A. Gazder, R. Hielscher, Parent grain reconstruction from partially or fully transformed microstructures in MTEX, J. Appl. Crystallogr. 55 (1) (2022) 180–194.
[45] V. Tong, S. Joseph, A.K. Ackerman, D. Dye, T.B. Britton, Using transmission Kikuchi diffraction to characterise $\alpha$ variants in an $\alpha$+ $\beta$ titanium alloy, J. Microsc. 267 (3) (2017) 318–329.
[46] L.A. Gatys, A.S. Ecker, M. Bethge, Image style transfer using convolutional neural networks, in: Proceedings of the IEEE Conference on Computer Vision and Pattern Recognition, 2016, pp. 2414–2423.
[47] X. Li, Y. Zhang, H. Zhao, C. Burkhart, L.C. Brinson, W. Chen, A transfer learning approach for microstructure reconstruction and structure-property predictions, Sci. Rep. 8 (1) (2018) 13461.
[48] I. Goodfellow, Y. Bengio, A. Courville, Deep Learning, MIT Press, 2016.
[49] K. Simonyan, A. Zisserman, Very deep convolutional networks for large-scale image recognition, 2014, arXiv preprint arXiv:1409.1556.
[50] P. Seibert, A. Raßloff, M. Ambati, M. Kästner, Descriptor-based reconstruction of three-dimensional microstructures through gradient-based optimization, Acta Mater. 227 (2022) 117667.
[51] M. Simonelli, Y.Y. Tse, C. Tuck, Effect of the build orientation on the mechanical properties and fracture modes of SLM Ti-6Al-4V, Mater. Sci. Eng.: A 616 (2014) 1–11.
[52] M.I. Latypov, M. Kühbach, I.J. Beyerlein, J.-C. Stinville, L.S. Toth, T.M. Pollock, S.R. Kalidindi, Application of chord length distributions and principal component analysis for quantification and representation of diverse polycrystalline microstructures, Mater. Charact. 145 (2018) 671–685.
[53] K.F. Mulchrone, K.R. Choudhury, Fitting an ellipse to an arbitrary shape: implications for strain analysis, J. Struct. Geol. 26 (1) (2004) 143–153.
[54] J. Ma, J. Tian, M. Yan, Z. Chen, J. Shen, J. Wu, Defect analysis and 2D/3D-EBSD investigation of an electron beam melted Ti-6Al-4V alloy, Mater. Charact. 166 (2020) 110440.